

Effect of La³⁺ Impurity on Magnetic and Electrical Properties of Co–Cu–Cr–Fe Nanoparticles

Vivek Chaudhari¹, R. H. Kadam², M. L. Mane³, Sagar E. Shirsath^{4,*},
A. B. Kadam⁵, and D. R. Mane¹

¹Dr. Babasaheb Ambedkar Marathwada University, Aurangabad 431004, MS, India

²Materials Research Laboratory, Srikrishna Mahavidyalaya Gunjoti, Omerga, Osmanabad, 413613, MS, India

³Department of Physics, S. G. R. G. Shinde Mahavidyalaya, Paranda 413502, MS, India

⁴Faculty of Engineering, Spin Device Technology Center, Shinshu University, Nagano 380-8553, Japan

⁵Department of Physics, Jawahar Mahavidyalaya, Andoor 413606, MS, India

In this work a series of Co_{0.7}Cu_{0.3}Cr_{0.5}La_xFe_{1.5-x}O₄ were synthesized via sol–gel auto-combustion technique through the incorporation of La³⁺ into the raw powders. The structural magnetic and resistivity properties of the synthesized Co–Cu–Cr–La ferrites were investigated. X-ray diffraction data indicated that, after La³⁺ doping, samples consisted of the main spinel phase in combination with a small amount of a foreign LaFeO₃ phase. The addition of La³⁺ resulted in the reduction of particle size and an increase of porosity of the synthesized samples. The infrared spectra were recorded on the range from 300–800 cm⁻¹. The two primary bands corresponding to tetrahedral ν_1 at 595–605 cm⁻¹ and octahedral ν_2 at 389–413 cm⁻¹ were observed. The octahedral site radii increased rapidly with La³⁺ substitution while the tetrahedral site radii slowly increased. Deviation from the ideal oxygen positional parameter is found to decrease with La³⁺ substitution. The saturation magnetization of the samples decreased with the amount of La³⁺ ions doped and the coercivity shows an opposite trend. La³⁺ substitution affects the hopping between Fe²⁺ ↔ Fe³⁺, resulted in increase in resistivity.

Keywords: Nanostructured Materials, Cation Distribution, IR, Magnetisation, Resistivity.

1. INTRODUCTION

Today, research on, and the manufacturing of, nanoparticles with sizes from a few nanometers up to micrometers have been introduced into many different applications including information carriers in biotechnology and medicine. In particular, magnetic nanomaterials represent one of the most exciting prospects in current nanotechnology. Magnetic nanoparticles of ferrites are of great interest in fundamental science, especially for addressing the fundamental relationships between magnetic properties and their crystal chemistry and structure.^{1–3}

Cobalt ferrite (CoFe₂O₄) a well-known hard ferrimagnetic material,⁴ in its bulk form crystallizes in mixed spinel structure with space group Fd3m. Mixed copper ferrites are also widely applied in inductors operating at high frequencies because their electrical resistivity is larger than

that of magnetic alloys by many orders of magnitude.⁵ Thermoelectric power studies of Cu–Cr ferrites as a function of composition and temperature have been studied by Venkateshwarlu and Ravinder.⁶ Structural, electrical and magnetic properties of Co–Cu ferrite nanoparticles have also been studied by various workers.^{7,8} Pure and mixed cobalt copper ferrites are of great interest due to their widespread application in electronics and medicine.⁹

There are a few reports available which have mentioned the synthesis of rare earth (RE³⁺) substituted nanocrystalline spinel ferrites in single phase form using different chemical routes despite having big difference in ionic radius of RE³⁺ and Fe³⁺ ions.^{10–14} La³⁺ is non-magnetic rare earth cation as it has no 4f electrons.¹⁵ However, its ionic size is much larger than the ionic size of Fe ions. So, little amount solid solution of La³⁺ in Co–Cu–Cr may create lattice strain in the material and it leads to modify the structure of the spinel ferrite. To the best of our knowledge there are no reports are available on the

*Author to whom correspondence should be addressed.

combination of Co–Cu–Cr ferrite with La³⁺ substitution. In this research we have made an attempt to study the effect of La³⁺ substitution on the structural, magnetic and electrical properties of Co_{0.7}Cu_{0.3}Cr_{0.5}La_xFe_{1.5-x}O₄ ($x = 0.0, 0.025, 0.05, 0.075, 0.1$).

2. EXPERIMENTAL DETAILS

The ferrite powders were synthesized through sol-gel auto-combustion¹⁶ route to achieve homogeneous mixing of the chemical constituents on the atomic scale and better sinterability. AR grade cobalt nitrate (Co(NO₃)₂ · 3H₂O), copper nitrate (Cu(NO₃)₂ · 6H₂O), chromium nitrate (Cr(NO₃)₃ · 9H₂O), lanthanum nitrate (La(NO₃)₃ · 6H₂O), iron nitrate (Fe(NO₃)₃ · 9H₂O) and citric acid (C₆H₈O₇ · H₂O), were used to prepare the Co_{0.7}Cu_{0.3}Cr_{0.5}La_xFe_{1.5-x}O₄ ($x = 0.0, 0.025, 0.05, 0.075, 0.1$) ferrite compositions. Reaction procedure was carried out in air atmosphere without protection of inert gases. The molar ratio of metal nitrates to citric acid was taken as 1:3. The metal nitrates were dissolved together in a minimum amount of double distilled water to get a clear solution. An aqueous solution of citric acid was mixed with metal nitrates solution, then ammonia solution was slowly added to adjust the pH at 7. Then the solution was heated at 90 °C to transform into gel. When ignited at any point of the gel, the dried gel burnt in a self-propagating combustion manner until all gels were completely burnt out to form a fluffy loose powder. The auto-ignition of gel was carried out in BOROSIL glass beaker upon a hot plate. The auto-combustion was completed within a minute, yielding the brown-colored ashes termed as a precursor. The as prepared powder then annealed at 600 °C for 4 h. Part of the powder was X-ray examined by Phillips X-ray diffractometer (Model 3710) using Cu-K_α radiation ($\lambda = 1.5405 \text{ \AA}$).

Transmission electron microscope (TEM) measurements were recorded on Philips (Model CM 200). The infrared spectra of all the samples were recorded at room temperature in the range 300 cm⁻¹ to 800 cm⁻¹ using Perkin Elmer infrared spectrophotometer. Room temperature magnetization of the samples was measured using the pulse field magnetization set-up. The DC electrical resistivity of all the samples was studied using two-probe technique. The measurements of DC electrical resistivity were taken in the temperature range 300–800 K on a disc shaped pellet of 10 mm diameter and 3 mm thickness.

3. RESULTS AND DISCUSSION

3.1. Structural Analysis

The annealed ferrites were characterized by XRD. Figure 1 shows the X-ray diffraction pattern of all the typical samples, indicating that all samples possess the cubic spinel structure (JCPDS card number 77-0013) with the appearance of weak peaks as secondary phases (LaFeO₃,

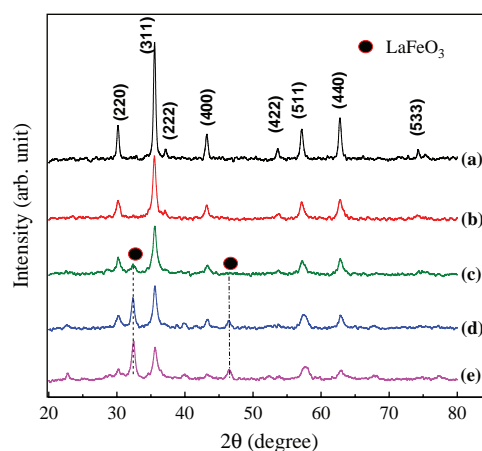


Figure 1. X-ray diffraction patterns of (a) $x = 0.0$, (b) $x = 0.025$, (c) $x = 0.050$, (d) $x = 0.075$ and (e) $x = 0.1$ for Co_{0.7}Cu_{0.3}Cr_{0.5}La_xFe_{1.5-x}O₄.

JCPDS card number 75-0541) for $x \geq 0.05$. The peak for LaFeO₃ increases with increasing La³⁺ substitution. The appearance of secondary phases in the La-substituted Co–Cu–Cr ferrites implies that the substitutes have a solubility limit in the spinel lattice. It is known that a degree of the replacement of Fe by the other ions in the spinel lattice depends on the cationic radius of the substitutes. Because the ionic radius of La³⁺ ions (1.05 Å) is larger compared to that of Fe³⁺ ions (0.67 Å), the replacement of Fe³⁺ by La³⁺ is limited in the spinel lattice, redundant La³⁺ ions form LaFeO₃ on the grain boundaries.¹⁷ The lattice parameter ‘*a*’ was calculated from the XRD data,¹⁸ shows the increasing trend from 8.387–8.403 Å with increase in La³⁺ substitution. The increase in lattice parameter with increasing La³⁺ content can be explained on the basis of the ionic radii. The ionic radius of La³⁺ is larger compared to Fe³⁺. Therefore, replacement of Fe³⁺ by La³⁺ will cause expansion of unit cell.

Figures 2(a) and (b) shows the TEM analysis of the synthesized powder the end samples. The particles tend to agglomerate because they experience a permanent magnetic moment proportional to their volume. The particle size of the synthesized powder is about 28–14 nm in size and exhibited more or less spherical morphology. It can be considered that La³⁺ ions may diffuse to the grain boundaries and form the secondary phase (orthoferrite) around the grains during the sintering process. This effect of segregation process on grain boundary will inhibit grain growth by limiting grain mobility.¹⁷ The HRTEM image (Fig. 2(c)) show the lattice fringes. The fringes of $d = 0.292 \text{ nm}$ (Fig. 2(c)) match that of the (220) plane of spinel phase. The corresponding SAED pattern (Fig. 2(d)) of the selected region indicates that the product is in amorphous nature due to the small particle sizes.

The bulk density ‘ d_B ’ of the specimens has been determined by the hydro-static method. The variation of the bulk density is shown in Figure 3. These measurements show density decreases from 4.539 to 4.418 g/cm³ with

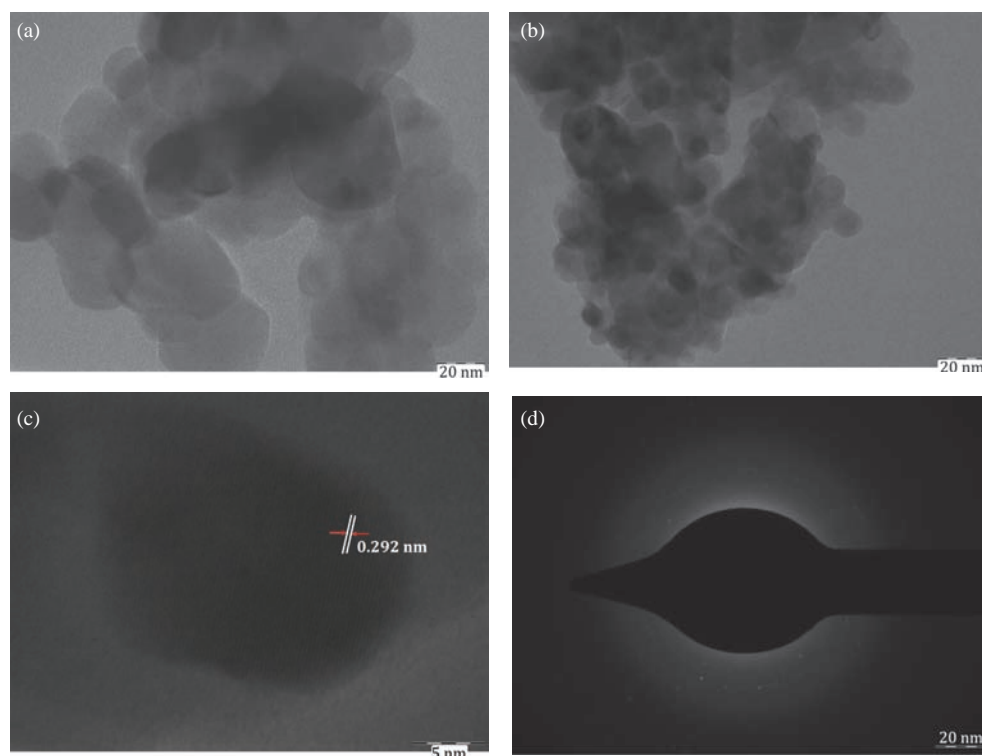


Figure 2. TEM images of (a) $x = 0.0$ and (b) $x = 0.1$ (c) HRTEM and (d) SAED pattern of $x = 0.1$.

increase in La³⁺ content which is in accordance with the densities of pure La and Fe, 6.162 g/cm³ and 7.874 g/cm³, respectively. Further, the bulk densities are related to the crystallite size, as the crystallite size decreases with La³⁺ ions which force to decrease in bulk density of the sample.

The percentage porosity is calculated using the following relation

$$P = \left(\frac{d_x - d_B}{d_x} \right) \times 100 \quad (1)$$

where d_x and d_B are the X-ray density and bulk density respectively. Figure 3 shows that the porosity increases with increase in La³⁺ substitution. The increase in porosity is related to decrease in crystallite diameter and bulk density.

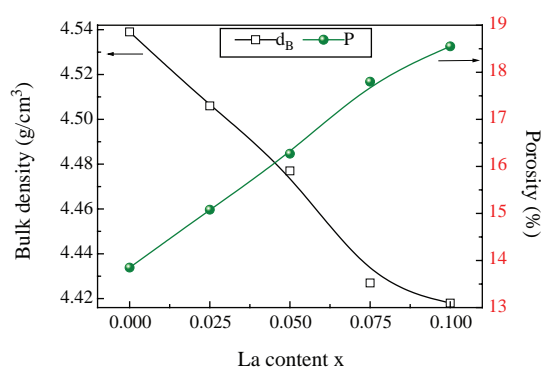


Figure 3. Variation of bulk density (d_B) and porosity (P) with La content x .

3.2. Infrared Spectroscopy

The room temperature IR spectra of the all the composition are shown in Figure 4. The spectra are recorded in the range from 300 to 800 cm⁻¹. The spectra show two main absorption bands at 600 cm⁻¹ and 400 cm⁻¹ as a common feature of all the ferrites. The high-frequency band ν_1 lies in the range 594–605 cm⁻¹ while the low-frequency band ν_2 is varying in the 389–413 cm⁻¹ range. The difference in the band position is expected because of the difference in Fe³⁺–O²⁻ distance for the octahedral and tetrahedral compounds. From the IR spectra it is noticed that the frequency ν_1 and ν_2 are shifted to higher frequencies with an increasing La³⁺ concentration and consequently with decreasing Fe ions concentration. The band positions for all the investigated composition are given in Table I. Waldron¹⁹ studied the vibration spectra of ferrites and attributed the ν_1 band to the intrinsic vibrations of the tetrahedral groups and ν_2 band to the octahedral groups. Thus, the replacement of La³⁺ with Fe³⁺ ions (having larger ionic radius and higher atomic weight than Fe³⁺) at octahedral site in the ferrite lattice affects the Fe³⁺–O²⁻ stretching vibration. This may be reason for the observed change in ν_1 and ν_2 band positions. It is also noted that the peak intensity slightly changes with an increasing La³⁺ content. It is known that the intensity ratio is a function of the change of dipole moment with the inter-nuclear distance ($d\mu/dr$).²⁰ This value represents the contribution of the ionic bond Fe–O in the lattice. So the observed decrease in the peak intensity with an increasing La³⁺ content is presumably due to

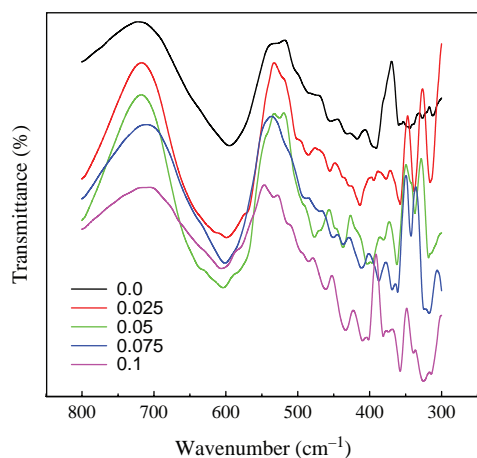


Figure 4. Infrared spectra of $\text{Co}_{0.7}\text{Cu}_{0.3}\text{Cr}_{0.5}\text{La}_x\text{Fe}_{1.5-x}\text{O}_4$.

the perturbation occurring in Fe—O bonds by substitution the La³⁺ ions.

3.3. Cation Distribution

The cation distribution in spinel ferrite can be obtained from the analysis of X-ray diffraction pattern. In the present work, the Bertaut method²¹ is used to determine the cation distribution. This method selects a few pairs of reflections according to the expression

$$\frac{I_{hkl}^{\text{Obs.}}}{I_{h'k'l'}^{\text{Obs.}}} = \frac{I_{hkl}^{\text{Calc.}}}{I_{h'k'l'}^{\text{Calc.}}} \quad (2)$$

where, $I_{hkl}^{\text{Obs.}}$ and $I_{hkl}^{\text{Calc.}}$ are the observed and calculated intensities for reflection (hkl), respectively. The best information on cation distribution is achieved when comparing experimental and calculated intensity ratios for reflections whose intensities

- (i) are nearly independent of the oxygen parameter,
- (ii) vary with the cation distribution in opposite ways and
- (iii) do not differ significantly.

The distribution of divalent and trivalent cations among octahedral and tetrahedral sites in the presently investigated samples were determined from the ratio of XRD lines I_{220}/I_{440} and I_{422}/I_{400} . These planes are assumed to be sensitive to the cation distribution. The temperature and absorption factors are not taken into account in our calculations as they do not affect the intensity calculation. If an agreement factor (R) is defined as in Eq. (3), the best-simulated structure which matches the actual structure of

Table I. IR absorption bands of $\text{Co}_{0.7}\text{Cu}_{0.3}\text{Cr}_{0.5}\text{La}_x\text{Fe}_{1.5-x}\text{O}_4$.

Comp. x	ν_1 (cm^{-1})	ν_2 (cm^{-1})
0	595	389
0.025	599	413
0.05	601	398
0.075	602	405
0.1	605	409

the sample will lead to a minimum value of R and the corresponding cation distribution is obtained for each hkl and $h'k'l'$ reflection pair considered,

$$R = \left| \left(\frac{I_{hkl}^{\text{Obs.}}}{I_{h'k'l'}^{\text{Obs.}}} \right) - \left(\frac{I_{hkl}^{\text{Calc.}}}{I_{h'k'l'}^{\text{Calc.}}} \right) \right| \quad (3)$$

For the calculation of the relative integrated intensity (I_{hkl}) of a given diffraction line from powder specimens as observed in a diffractometer with a flat-plate sample holder, the following formula is valid,

$$I_{hkl} = |F|_{hkl}^2 P \cdot L_P \quad (4)$$

where, F is the structure factor, P is the multiplicity factor, L_P is the Lorentz-polarization factor and

$$L_P = \frac{1 + \cos^2 2\theta}{\sin^2 \theta \cos \theta} \quad (5)$$

The atomic scattering factors for various ions were taken from the literature.¹⁸

It should be added that the calculated integrated intensities are valid at 0 K. Because the observed values are obtained at room temperature, a suitable correction is in principle necessary for precise comparison. However, the spinels are high-melting compounds, the thermal vibration of the atoms at room temperature should not differ greatly from that at absolute zero. Therefore, in our intensity calculations no temperature correction was deemed necessary.

The cation distribution from in above mentioned way is listed in Table II. From the data of cation distribution we conclude that the La³⁺ ions show a preference for octahedral sites. From occupancy variation we have observed that Co²⁺ ion can occupy both tetrahedral and octahedral sites. Hence, the present samples are in mixed spinel structure. Radius of the octahedral site is larger than the tetrahedral site in the spinel lattice. The ionic radius of the La³⁺ ion is large enough for octahedral site. One can assume that small amount of La³⁺ cations can be substituted for Fe³⁺ cations which enter into the octahedral sites by rearrangement of cations between the tetrahedral and octahedral sites to minimize the free energy of the system. Partial migration of Co²⁺ ions (0.78 Å) from B to A sites has been observed by increasing the La concentration accompanied by an opposite transfer of equivalent number of Fe³⁺ ions (0.67 Å) from A to B sites in order to relax the strain at

Table II. Cation distribution of $\text{Co}_{0.7}\text{Cu}_{0.3}\text{Cr}_{0.5}\text{La}_x\text{Fe}_{1.5-x}\text{O}_4$.

Comp. x	A-site				B-site				
	Co	Cu	Cr	Fe	Co	Cu	Cr	La	Fe
0	0.1	0	0.1	0.8	0.6	0.3	0.4	0	0.7
0.025	0.105	0.004	0.1	0.791	0.595	0.296	0.4	0.025	0.684
0.05	0.11	0.008	0.1	0.782	0.59	0.292	0.4	0.05	0.668
0.075	0.115	0.012	0.1	0.773	0.585	0.288	0.4	0.075	0.652
0.1	0.12	0.016	0.1	0.764	0.58	0.284	0.4	0.1	0.636

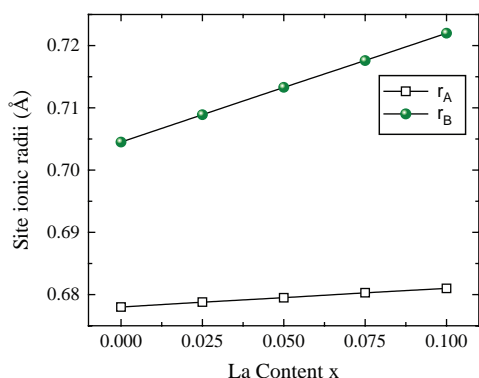


Figure 5. Variation of site ionic radii (r_A and r_B) with La content x .

the octahedral sites.²² Cu²⁺ and Cr³⁺ ions showed a strong preference for the octahedral B -site due to favorable fit of charge distribution. The mean ionic radius of the A and B sites (r_A and r_B) can be calculated for all the samples using the relations discussed elsewhere.^{23,24} It is observed from Figure 5 that r_A and r_B increases with increase in La³⁺ substitution. The increase in r_B is due to the replacement of smaller Fe³⁺ ions of ionic radii (0.67 Å) by larger La³⁺ ions with 1.05 Å ionic radii at octahedral B -site. The small increase in r_A is due to the migration of Cu²⁺ and Co²⁺ ions from B site to A site, that force to increase the octahedral radii.

The theoretical values of lattice parameter can be calculated with the help of following equation,²⁵

$$a_{th} = \frac{8}{3}\sqrt{3}[(r_A + R_0) + \sqrt{3}(r_B + R_0)] \quad (6)$$

where r_A and r_B are radii of tetrahedral (A) site and octahedral [B] site, r_O is radius of oxygen i.e., ($r_O = 1.32$ Å). The variation of theoretical lattice constant as shown in Figure 6 is similar to that observed for experimentally determined lattice parameter.

Using the values of ' a ', the radius of oxygen ion $R_0 = 1.32$ Å and ' r_A ' in the following expression, the oxygen positional parameter ' u ' can be calculated,²³

$$u = \left[(r_A + R_0) \frac{1}{\sqrt{3}a} + \frac{1}{4} \right] \quad (7)$$

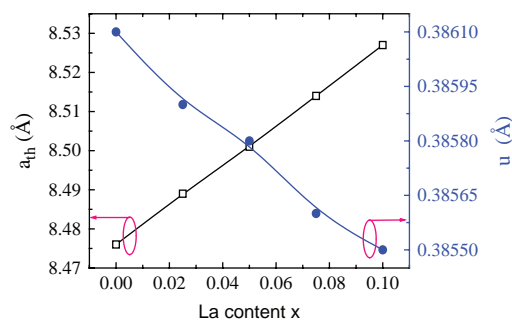


Figure 6. Variation of theoretical lattice constant (a_{th}) and oxygen parameter (u) with La content.

Figure 6 shows the variation of oxygen positional parameter ' u ' with La³⁺ substitution. In most oxide spinels the oxygen ions are apparently larger than the metallic ions. In spinel like structure the oxygen positional parameter has a value in the neighborhood of 0.375 Å for which the arrangement of O²⁻ ions are equals exactly a cubic closed packing but in actual spinel lattice, this ideal pattern is slightly deformed. The u has a value 0.375 Å when the origin is chosen on the tetrahedral sites but the structure is a centric and the structure factor calculation is less direct.²⁴ Our value of ' u ' is larger than its ideal value ($u = 0.375$ Å), this larger value may probably be due to many reasons, including the history of the samples, experimental or measurement errors, e.g., precision of the observed X-ray intensity and the theoretical data used for the scattering model of the system.

3.4. Magnetization

The magnetization curves of the synthesized samples of La-substituted Co–Cu–Cr ferrites obtained at room temperature VSM measurement are shown in Figure 7. Absence of good hysteresis, and the non-attainment of saturation at a high applied magnetic field of 11 kOe indicate the presence of superparamagnetic behavior. Addition of La³⁺ ions into Co–Cu–Cr ferrite greatly affects its magnetic properties. It is observed from Figures 7 and 9 that magnetization decreases with increase in La³⁺ substitution. In spinel ferrite the saturation magnetization is dominated by the superexchange interactions between the tetrahedral (A -sites) and octahedral (B -sites) sites cations. La³⁺ ions do not take part in the exchange interactions to the nearest neighboring ions as they are non-magnetic. Hence it will decrease the number of magnetic linkages occurring between tetrahedral and octahedral cations. It leads to weakening of the tetrahedral–octahedral superexchange interactions with the increase in La³⁺ concentration.²⁵ The addition of nonmagnetic ions in the ferrites suppressed the A -interaction and developed a B – B interaction, which is reflected in reducing the saturation magnetization.²⁶ Furthermore, the deformity of the spinel lattice and increasing

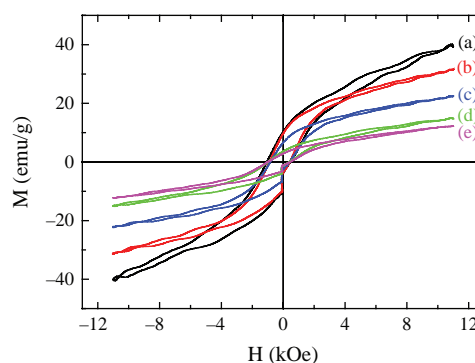


Figure 7. Variation of magnetization with applied field, where (a) $x = 0.0$, (b) $x = 0.025$, (c) $x = 0.050$, (d) $x = 0.075$ and (e) $x = 0.1$.

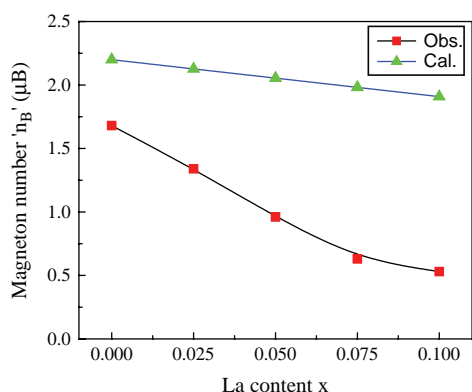


Figure 8. Variation of observed (Obs.) and calculated (Cal.) magneton number with La content x .

the nonlinear antiferromagnetic coupling between A and B sublattice due to La³⁺ substitution, decreases the saturation magnetization of samples.²⁷ According to Neel's molecular-field model,²⁸ the A – B super exchange interaction predominate the intrasublattice A – A and B – B interactions. Therefore, the net magnetic moment is given by the sum of the magnetic moments of the A and B sublattices.

The magnetic moment per formula unit (n_B) was calculated from Neel's sub-two-lattice model using the relation,

$$n_{\text{Bcal.}} = M_B(x) - M_A(x) \quad (8)$$

where M_B and M_A are the B and A sub-lattice magnetic moments in μ_B . The $n_{\text{Bcal.}}$ (μ_B) values for the present system were calculated using cation distribution (Table II) and the ionic magnetic moment of Fe³⁺, Co²⁺, Cu²⁺, Cr³⁺ and La³⁺ with their respective values $5\mu_B$, $3\mu_B$, $1\mu_B$, $3\mu_B$ and $0\mu_B$. The variation of calculated magneton number is shown in Figure 8. In the present ferrite system the Fe³⁺ ions are replaced by La³⁺ ions, leading to a decrease in the B -site sublattice magnetization. Therefore, the magnetization of the B sublattices decreases, which leads to a decrease in the net magnetization (Fig. 7). The decrease in magneton number is explained by the A – B interaction. In the present case, La³⁺ ions of non-magnetic moment replaces Fe³⁺ ions of high magnetic moment ($5\mu_B$). According to the cation distribution data from Table II, La³⁺ ions occupy octahedral B -sites. This placement leads to a decrease of the magnetic moment of the B -site, and thus the magneton number n_B decreases with La substitution.

The observed magnetic moment per formula unit in the Bohr magneton (μ_B) was calculated using a relation;²⁹

$$n_B = \frac{M_w \times M_s}{5585} \quad (9)$$

where M_w is the molecular weight and M_s is the saturation magnetization of the samples. It is obvious from Figure 8 that the calculated and observed values of the magneton number are in good agreement with each other.

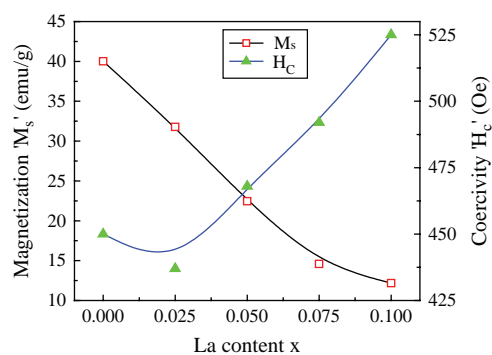


Figure 9. Variation of magnetization and coercivity with La content x .

Figures 7 and 9 shows that the coercivity (H_c) increased as the La³⁺ content increases, similarly to porosity. Porosity affects the magnetization process because the pores work as a generator of a demagnetizing field. As the porosity increases, a higher field is needed to push the domain wall, increasing H_c . The saturation magnetization is related to H_c through Brown's relation,³⁰

$$H_c = \frac{2K_1}{\mu_0 M_s} \quad (10)$$

According to this relation, H_c is inversely proportional to M_s , which is consistent with our experimental results. It is also to be noted that the coercivity is a microstructure property. It depends upon defects, surface effect, strains, non-magnetic atoms, etc. in the material.³¹ The coercive force variation of the system shows a typical size dependent behavior. This behavior can be attributed to the combination of surface effect and its surface anisotropy.³² The electronic configuration of La³⁺ ions results in the lattice or crystalline field distortion, and generates an internal stress. Also, the strong spin-orbit coupling of rare earth La³⁺ ions may contribute to the anisotropy, when they are located in the B sites of ferrite.³³ This might also one of the reasons to increase the coercivity of the samples with La³⁺ doping.

3.5. DC Resistivity

The dc resistivity of the samples was measured using the two-probe method where silver is used as a contact material. For measuring temperature varying current, the sample is firmly fixed between two electrodes. An auxiliary heater is used for heating of all investigated samples. The temperature was measured using a chromel-alumel thermocouple. The accuracy in resistivity measurements were about 2% respectively. Figure 10 shows the variations in DC resistivity with La³⁺ substitution. The substitutions of La³⁺ ions have resulted in higher DC resistivities. The reduction of Fe³⁺ ions with every La³⁺ substitution may reduce the hopping between iron ions such as Fe²⁺ ↔ Fe³⁺ in octahedral sites and contributes to increase the resistivity slightly for all the compositions in the system.

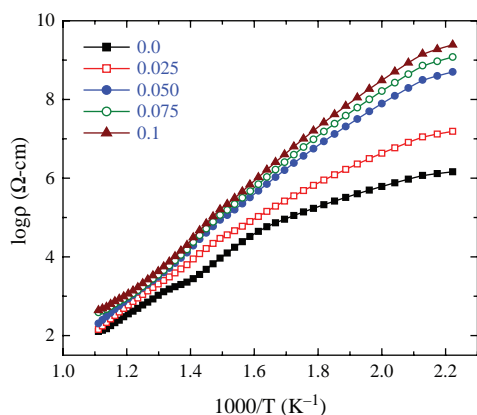


Figure 10. Variation of resistivity with temperature.

Further, the La³⁺ ions at *B*-sites do not participate in the conduction processes, but limit the degree of conduction by acting as scattering centres in the sense that they reduce the number of Fe³⁺ ions. The total number of iron ions present at *B*-sites decreases with every step of La³⁺ substitution and also the available Fe²⁺ ions for hopping at these sites decrease in number; thus, under the situation, it may lead to balance the quantities of Fe²⁺ and Co²⁺/Cu²⁺ ions to lock-up effectively and result in higher resistivities. It is observed that for all the samples resistivity decreases with increasing temperature, indicating the semi-conducting nature of the samples. The temperature dependence of resistivity found to follow the Arrhenius equation,

$$\rho = \rho_0^{-\frac{E_g}{k_B T}} \quad (11)$$

where ρ_0 is the pre-exponential factor with the dimensions of $\Omega\text{-cm}$, k_B is the Boltzmann constant (8.6173439×10^{-5} eV/K), E_g is the activation energy, and T is the absolute temperature. The conduction mechanism of ferrites can be explained on the basis of the Verwey de Boer³⁴ mechanism that involves exchange of electrons between the ions of the same elements present in more than one valence state and distributed randomly over crystallographic lattice sites. The decrease in resistivity with increase in temperature is due to the increase in drift mobility of the charge carriers. Also conduction in ferrites is attributed to hopping of electrons of iron ions such as $\text{Fe}^{2+} \leftrightarrow \text{Fe}^{3+}$ at elevated temperatures. It can be seen that for all the samples variation of resistivity with increasing temperature follow the same trend. For spinel ferrite samples usually three linear regions are observed in the $\log \rho$ versus $1000/T$ plot from room temperature to well above Curie temperature.^{35–37} The change in slope indicates change in conduction mechanism. The first low-temperature region is attributed to the conduction due to impurities, voids, defects, etc. The second temperature region (up to Curie temperature) is attributed to ferrimagnetic region. Third temperature region (above Curie temperature) is attributed to paramagnetic region.^{36,37} In the

present case second and third region agrees with the reports in the literature.

4. CONCLUSIONS

La³⁺ substituted Co–Cu–Cr ferrites nanoparticles with a chemical formula $\text{Co}_{0.7}\text{Cu}_{0.3}\text{Cr}_{0.5}\text{La}_x\text{Fe}_{1.5-x}\text{O}_4$ were successfully synthesized via the sol–gel method. The incorporation of lanthanum was found to affect the structural, magnetic and electrical properties. Lattice constant found to increase with the increase in La³⁺ ions, this increase in lattice constant is related to ionic radii of La³⁺ ions. The average crystallite size decreases with increase in La³⁺ substitution. FT-IR spectra assumed the octahedral preferential occupancy of the lanthanum ions. The cation distribution suggests that Cu²⁺, Cr³⁺ and La³⁺ have strong preference towards octahedral *B*-site, whereas Co²⁺ and Fe³⁺ ions are distributed over both the lattice sites. The theoretical lattice constant and experimental lattice constant matches each other very well. Hysteresis loop measurements indicated a decrease in the measured saturation magnetization with increasing La³⁺ substitution. This behavior is ascribed to the fact that the increasing concentration of nonmagnetic La³⁺ ions weakens the inter-site exchange interaction, decreasing the value of saturation magnetization. Resistivity increases with increase in La³⁺ substitution, this suggest the reduction in hopping of electron between Fe²⁺ and Fe³⁺ ions.

References and Notes

1. A. Goldman, *Modern Ferrite Technology*, 2nd edn., Springer, New York (2006).
2. A. Kleinauskas, J.-K. Kim, G.-H. Choi, H.-T. Kim, K. Røe, and P. Juzenas, *Rev. Nanosci. Nanotechnol.* 1, 271 (2012).
3. Y. Hao, S. Song, X. Yang, J. Xing, and J. Chen, *J. Nanosci. Nanotechnol.* 12, 7716 (2012).
4. R. Krishna, E. Titus, S. Chandra, N. Bardhan, R. Krishna, D. Bahadur, and J. Gracio, *J. Nanosci. Nanotechnol.* 12, 6631 (2012).
5. Z. Huang, G. Yin, X. Liao, Y. Yao, and Y. Kang, *J. Coll. Inter. Sci.* 317, 530 (2008).
6. Ch. Venkateswarlu and D. Ravinder, *J. Alloys Compd.* 397, 5 (2005).
7. D. R. Mane, D. D. Birajdar, S. Patil, S. E. Shirsath, and R. H. Kadam, *J. Sol–Gel Sci. Technol.* 58, 70 (2011).
8. Mohd. Hashim, Alimuddin, S. Kumar, B. H. Koo, S. E. Shirsath, E. M. Mohammed, J. Shah, R. K. Kotnala, H. K. Choi, H. Chung, and Ravi Kumar, *J. Alloys Compd.* 518, 11 (2012).
9. S. Gautam, S. Muthurani, M. Balaji, P. Thakur, D. Pathinettam Padiyan, K. H. Chae, S. S. Kim, and K. Asokan, *J. Nanosci. Nanotechnol.* 11, 386 (2011).
10. S. E. Shirsath, R. H. Kadam, S. M. Patange, M. L. Mane, A. Ghasemi, and A. Morisako, *Appl. Phys. Lett.* 100, 042407 (2012).
11. A. Rana, V. Kumar, O. P. Thakur, and R. P. Pant, *J. Nanosci. Nanotechnol.* 12, 6355 (2012).
12. L. Zhao, Y. Cui, H. Yang, L. Yu, W. Jin, and S. Feng, *Mater. Lett.* 60, 104 (2006).
13. I. M. Obaidat, B. Issa, and Y. Haik, *J. Nanosci. Nanotechnol.* 11, 3882 (2011).

14. L. B. Tahar, M. Artus, S. Ammar, L. S. Smiri, F. Herbst, M. J. Vaulay, V. Richard, J. M. Greneche, F. Villian, and F. Fievet, *J. Magn. Magn. Mater.* 320, 3242 (2008).
15. R. Valenzuela, *Magnetic Ceramics*, Cambridge University Press, Cambridge (1994).
16. N. R. Panchal and R. B. Jotania, *Nanosci. Nanotechnol. Lett.* 4, 623 (2012).
17. X. Zhou, J. Jiang, L. Li, and F. Xu, *J. Magn. Magn. Mater.* 314, 7 (2007).
18. B. D. Cullity, *Elements of X-Ray Diffraction*, Addison-Wesley, London (1959).
19. R. D. Waldron, *Phys. Rev.* 99, 1727 (1955).
20. S. A. Mazen, M. H. Abdallah, B. A. Sabrah, and H. A. M. Hashem, *Phys. Stat. Sol. (a)* 134, 263 (1992).
21. L. Weil, F. Bertaut, and L. Bochirol, *J. Phys. Radium* 11, 208 (1950).
22. L. Kumar and M. Kar, *Ceram. Inter.* 38, 4771 (2012).
23. K. J. Standley, *Oxide Magnetic Materials*, Clarendon Press, Oxford (1972).
24. G. Fagherazzi and F. J. Garbassi, *J. Appl. Cryst.* 5, 18 (1972).
25. J. Jacob and M. A. Khadar, *J. Appl. Phys.* 107, 114310 (2010).
26. H. M. Zaki and S. Al-Heniti, *J. Nanosci. Nanotechnol.* 12, 7126 (2012).
27. J. Jing, L. Liangchao, and X. Feng, *J. Rare Earths* 25, 79 (2007).
28. L. Néel, *Ann. Phys. Paris* 3, 137 (1948).
29. J. Smit and H. P. J. Wijn, *Ferrites*, Philips Technical Library, Eindhoven, The Netherlands (1959).
30. J. M. D. Coey, *Rare Earth Permanent Magnetism*, John Wiley and Sons, New York (1996).
31. P. K. Roy and J. Bera, *J. Magn. Magn. Mater.* 320, 1128 (2008).
32. S. E. Shirsath, R. H. Kadam, A. S. Gaikwad, A. Ghasemi, and A. Morisako, *J. Magn. Magn. Mater.* 323, 3104 (2011).
33. F. X. Cheng, J. T. Jia, Z. G. Xu, B. Zhou, C. S. Liao, and C. H. Yan, *J. Appl. Phys.* 86 2727 (2007).
34. E. J. Verwey and J. H. de Boer, *Rec. Trans. Chim. Phys. Bas.* 55, 531 (1936).
35. B. Vishwanathan and V. R. K. Murthy, *Ferrite Materials: Science and Technology*, Narosa Publication House, New Delhi (1990).
36. Y. L. Liu, Z. M. Liu, Y. Yang, H. F. Yang, G. L. Shen, and R. Q. Yu, *Sens. Actuators B* 107, 600 (2005).
37. S. Solyman, *Ceram. Int.* 32, 755 (2006).

Received: 28 November 2012. Accepted: 30 January 2014.

Delivered by Publishing Technology to: McMaster University
IP: 159.16.249.228 On: Thu, 21 Jan 2016 15:08:16
Copyright: American Scientific Publishers